High Power Laser Science and Engineering, (2023), Vol. 11, e51, 12 pages.
doi:10.1017/hpl.2023.33

HIGH POWER LASER SCIENCE AND ENGINEERING

RESEARCH ARTICLE

Synchronous post-acceleration of laser-driven protons in helical coil targets by controlling the current dispersion

Zhipeng Liu[1], Zhusong Mei[1], Defeng Kong[1], Zhuo Pan[1], Shirui Xu[1], Ying Gao[1], Yinren Shou[1], Pengjie Wang[1], Zhengxuan Cao[1], Yulan Liang[1], Ziyang Peng[1], Jiarui Zhao[1], Shiyou Chen[1], Tan Song[1], Xun Chen[1], Tianqi Xu[1], Xueqing Yan[1,2,3], and Wenjun Ma[1,2,3]

[1] *State Key Laboratory of Nuclear Physics and Technology, and Key Laboratory of HEDP of the Ministry of Education, CAPT, Peking University, Beijing, China*

[2] *Beijing Laser Acceleration Innovation Center, Beijing, China*

[3] *Institute of Guangdong Laser Plasma Technology, Guangzhou, China*

(Received 9 December 2022; revised 1 March 2023; accepted 31 March 2023)

Abstract

Post-acceleration of protons in helical coil targets driven by intense, ultrashort laser pulses can enhance ion energy by utilizing the transient current from the targets' self-discharge. The acceleration length of protons can exceed a few millimeters, and the acceleration gradient is of the order of GeV/m. How to ensure the synchronization between the accelerating electric field and the protons is a crucial problem for efficient post-acceleration. In this paper, we study how the electric field mismatch induced by current dispersion affects the synchronous acceleration of protons. We propose a scheme using a two-stage helical coil to control the current dispersion. With optimized parameters, the energy gain of protons is increased by four times. Proton energy is expected to reach 45 MeV using a hundreds-of-terawatts laser, or more than 100 MeV using a petawatt laser, by controlling the current dispersion.

Keywords: current dispersion; helical targets; laser-driven ions; synchronous post-acceleration

1. Introduction

Ion acceleration driven by intense and ultrashort laser pulses[1,2] has attracted increasing attention as it can produce MeV–GeV ions on micrometer scale. The unique properties of laser-driven ions, such as ultra-high peak current[3,4] and small source size[5], are in high demand for applications such as radiography[6], FLASH radiotherapy[7,8], material science[9] and nuclear fusion[10]. Among the acceleration mechanisms proposed so far, the most rigorously studied mechanism is target normal sheath acceleration (TNSA)[11–13]. When an ultra-intense laser pulse irradiates a thin solid target, energetic electrons are generated on its front surface. These hot electrons then penetrate the target and create a substantial charge-separation electric field on the target's rear surface. Ions can be accelerated in this electric field to high energy in a few micrometers. It has been identified as a robust method that can stably generate proton beams with maximum energy up to several tens of MeV[14]. However, theoretical models[15] and experimental results[16,17] have motivated the scaling law between TNSA accelerated ion beam energy and laser intensity as $E_{\mathrm{ions}} \propto I_{\mathrm{laser}}{}^{1/2}$, indicating that it is highly difficult, if possible, to obtain hundreds of MeV protons at the currently available laser intensity[18–20].

To overcome the predicament of TNSA acceleration, Kar *et al.*[21] proposed and realized a scheme for simultaneous post-acceleration, energy selection and ion collimation by attaching a sub-millimeter-diameter helical coil (HC) normal to the rear side of the metallic target foil. It is a further use of the electrons escaping from the laser-ion acceleration without the need for an extra laser pulse. In typical TNSA, the intense laser pulse irradiates the target surface and creates energetic electrons that partially escape. Electrons have a picosecond-scale duration and charge of a few to hundreds of nC[22]. As the escaping electrons leave a positive charge

Correspondence to: Wenjun Ma, State Key Laboratory of Nuclear Physics and Technology, and Key Laboratory of HEDP of the Ministry of Education, CAPT, Peking University, Beijing 100871, China. Email: wenjun.ma@pku.edu.cn

on the target, a discharge current is driven along the wire at a speed close to c, the speed of light in a vacuum[23,24]. This current has an ultra-high density of μC m^{-1}, which can generate an electromagnetic pulse (EMP) along the wire[25,26]. The helical wire acts as an electromagnetic field (EMF) guide to form an intense electric field with a magnitude of GV/m in the center of the HC[21] to post-accelerate the TNSA proton beam. In a demonstration experiment of HC post-acceleration (HCPA), where a 200 TW laser system was used, the maximum proton energy was increased by 35% (2.7 MeV) using a 7-mm-long HC. Later work by Ahmed *et al.*[27] highlighted HCPA's function in beam focusing and energy spectrum modulation. They obtained a highly collimated ($<1^\circ$ divergence angle) and narrow-band (10% energy spread) proton beam at approximately 10 MeV. The energy gain can be more significant with increased laser energy and intensity. Simulations based on a test-particle approach predict that a single HC can boost proton energy by 30 MeV with a PW laser[21]. However, the experimental results showed that the energy gain was not as high as expected: only 12 MeV enhancement was observed[28].

Prolonging the acceleration distance by maintaining the synchronization of the HCPA field and protons would be a practical way to increase the energy gain in experiments. Kar *et al.*[21] conceived a two-beam laser-triggered HC current, allowing protons to travel through the HC twice, and the maximum energy in the simulation exceeded 100 MeV. This scheme was experimentally implemented by Ferguson *et al.*[29]. Two laser beams with energies of approximately 50 J and approximately 60 J, respectively, interact with two coil targets sequentially. By precisely controlling the beam injection, the protons were post-accelerated twice with an energy gain of approximately 16 MeV (~8 MeV per stage). Moreover, it was proposed that acceleration can synchronize the electric field and accelerating ions by continuously or stepwise adjusting the pitch and radius of the HC[28]. However, it is difficult to implement this HC structure experimentally.

In the above works, the current propagating in the HC was assumed to be dispersionless. As a matter of fact, picosecond transient current has a frequency spectrum as wide as tens of GHz[30–33]. When such a broadband current propagates along an HC, the dispersion affected by coupled inductances and capacitances is nonnegligible. Bardon *et al.*[34] found that in the simulation, the velocity dispersion of the current leads to progressive modification of HCPA, which may be one of the most important reasons for the termination of acceleration in a long HC. Since previous experiments and simulations did not consider current dispersion, an in-depth investigation of its effect on long-time synchronization between the post-acceleration field and protons is important.

In this paper, we systematically study HCPA considering the dispersion effect by using self-consistent EMF and beam dynamics simulations. We first illustrate the relationship between the dispersed current and electric field and its impact on proton beam dynamics, which provides important insight into HCPA. It is found that the sudden phase reversal of the electric field induced by the current dispersion is the primary reason for the termination of HCPA. Based on our understanding, we propose a two-stage HC structure to compensate for phase change. Under controlled synchronization between the acceleration field and protons, HCPA energy gain is increased by four times.

The paper is structured as follows. Section 2 describes the setup and method of large-scale self-consistent simulations for the current and EMFs. In Section 3, we present the dispersion of current in a straight wire and HC and explain it with a circuit transmission model. In Section 4, we analyze the evolution of the electric field and post-acceleration of protons in a single-stage HC, and demonstrate how current dispersion leads to asynchrony of the electric field and proton beam. In Section 5, we propose a dispersion controlled two-stage HC scheme to enhance energy gain. In Section 6, we discuss the scheme using a multi-stage HC (more than two), and find that additional stages are not beneficial for further energy enhancement. Section 7 summarizes our results.

2. Simulation method

Several numerical simulation methods of HCPA have been reported previously. Jiang *et al.*[35] executed particle-in-cell (PIC) simulations of the laser's interaction with an ionized tens-of-micrometers solenoid target. However, these explicit PIC simulations would be unacceptable for such a large HC target (a few centimeters) due to computational limitations. Ahmed *et al.*[27,28] and Kar *et al.*[21,36] used the particle-tracing code to investigate proton dynamics, where EMP propagation in the HC is treated as a transverse electromagnetic (TEM) mode. The phase velocity and group velocity of the EMP are equal and independent of frequency, and the HC is considered a dispersionless medium. Bardon *et al.*[34] used finite-difference time-domain (FDTD) codes[37,38] to simulate the current propagation through the HC, which is a suitable approach to simulate the EMF at full-scale (nanosecond and centimeter scales). However, their simulations lacked particle dynamics analysis to reveal the effect of velocity dispersion on post-acceleration.

Here, we employ the CST particle studio suite[39], a method that combines the FDTD and the PIC codes to simulate the EMFs and beam dynamics in HCPA. The PIC simulations initialize the velocity and position of the charged particles, and Maxwell's equations are solved by using the FDTD methods to obtain the EMFs efficiently. The EMFs and the particle dynamics are self-consistently described because all the terms in Maxwell's equations are retained in the equation scheme[40]. The generation of fast

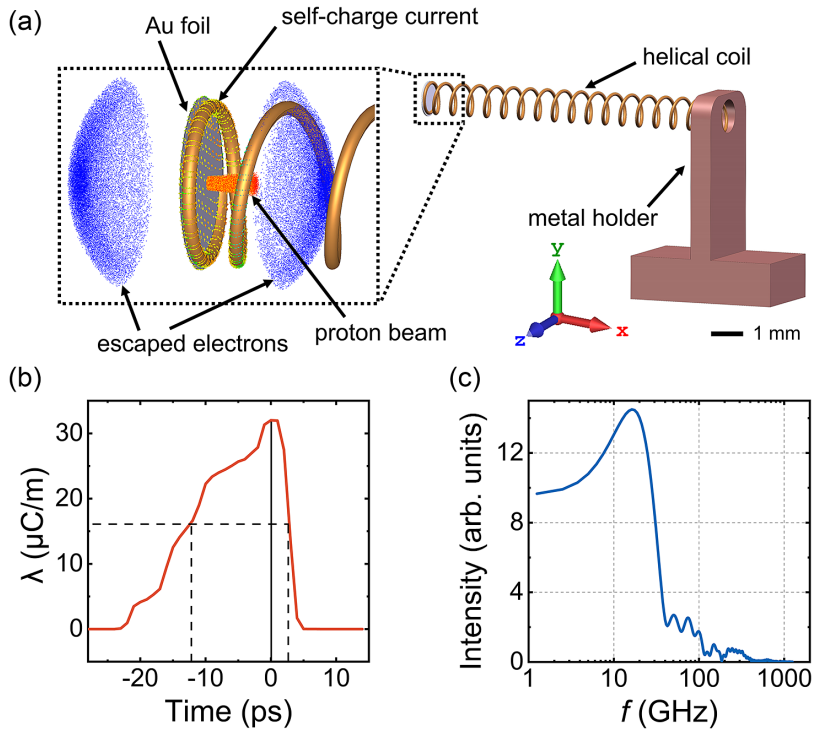

Figure 1. (a) Simulation setup of HC target configurations. (b) Self-discharged current generated by the emitted particles. (c) Spectrum of the current pulse from fast Fourier transform (FFT).

electrons and protons caused by the laser–plasma interaction (LPI) at the irradiation spot, which may require explicit PIC simulation, is simplified as particle source emission with energy distribution and total number subject to the interaction mechanism[23]. As a result, the discharged current will be excited spontaneously and propagate following Maxwell's equations. The interaction between the emitted particles and the generated EMFs is self-consistent, and both spatial-temporal profiles of the EMFs and proton dynamics can be specified.

To make the simulation more realistic, we perform full-scale simulations in time and space at the nanosecond and centimeter scales. The simulation configurations are shown in Figure 1(a). The foil target (Au, 10 μm thickness) is coaxially attached to the HC (aluminum, 100 μm wire diameter). All adjacent structures touch each other and are connected to a pure copper holder at the end to form a current path. All the materials are set as lossy metal, where the electrical conductivity and resistance are determined by the specific materials. Surface permittivity is considered in lossy metal as a surface impedance and skin effect. Nonlinearity is higher than the third-order and susceptibility is described as true third-order tensors in CST code[41]. The solver's frequency range is 0–100 GHz. The components of the target, coil and holder are meshed in high density with the cell size $\Delta x = \Delta y = \Delta z = 10$ μm. The entire simulation volume is 45 cm^3. Electrons and protons are modeled with 10 million macroparticles. The energy distribution of the proton beam is a Maxwellian function with an effective temperature $T_\mathrm{p} = 3.5$ MeV and cut-off energy $E_{\mathrm{p,cut-off}} = 25$ MeV. The energy spectrum of escaped electrons is a Maxwellian function with $T_\mathrm{e} = 2.5$ MeV and $E_{\mathrm{e,cut-off}} = 25$ MeV, close to that of other reported works[42,43]. The proton and electron divergence angles are set to 8° and 40°[44,45], respectively. The total charges of the escaped electrons and protons are 132 and 10 nC, respectively. As predicted by the model in Refs. [46–48], the protons' energy and electrons' charge could be achieved using a hundreds-of-terawatts femtosecond laser at an intensity of 8×10^{20} W cm^{-2}. The $\mathrm{d}N_{\mathrm{p,e}}/\mathrm{d}t$ of the emission time is negligible compared with the total simulation time. As the electrons and ions escape, a self-discharged current is generated in the wire. Figure 1(b) shows the simulated temporal profile of the current. The peak charge density is 32 μC m^{-1} and the pulse duration is 14 ps. In Figure 1(c), the spectrum of the current pulse is derived from fast Fourier transform (FFT), which has the main frequency of approximately 15 GHz and a range as wide as GHz–THz, similar to the reference results[46].

3. Dispersion of a transient current in a straight wire and a helical coil

Firstly, we simulate the propagation of a transient current on a straight Al wire. Figure 2(a) shows the simulation result of the current as a function of time. The front of

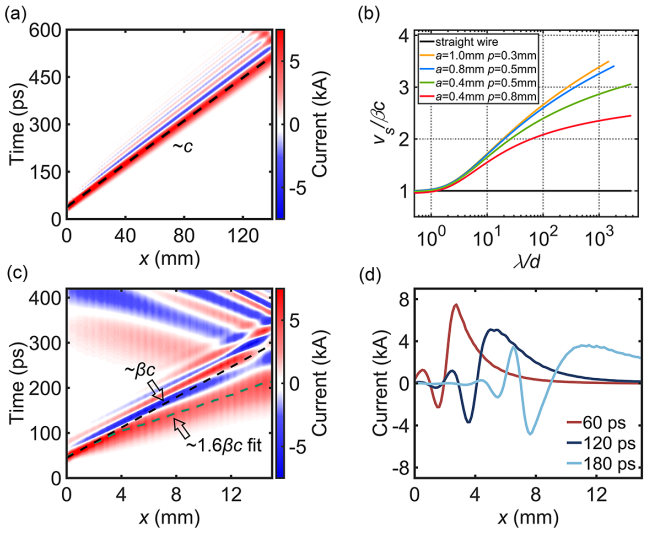

Figure 2. (a) The spatial-temporal distribution of the current on the straight aluminum wire, where the black dashed line refers to the speed of light. (b) Dependence of the surface current velocities on the ratio of the wavelength to the coil diameter (λ/d), with different radii and pitches in the HC and straight wire. The β and d are both set to 1 in the case of straight wire. (c) Distribution of current in the HC, with the velocity mark of βc (black dashed line) and the fitting longitudinal velocity $1.6\beta c$ of the main positive peak (green dashed line). (d) Snapshot of the current distributions in the HC at 60, 120 and 180 ps.

the current propagates along the wire near the speed of light in a vacuum. As it propagates in the x direction, the tail of the current grows due to dispersion. This can be numerically explained by the circuit transmission model[49]. To help clearly understand the impact of current dispersion, we assume that the transmission line is lossless, where resistance and conductance are set to zero. The nonlinear permittivity between the wire surface and the vacuum is ignored. The propagation of current can be described by the telegraph equation[50]:

$$\frac{\partial^2 J(x,t)}{\partial x^2} = LC\frac{\partial^2 J(x,t)}{\partial t^2}, \tag{1}$$

where $J(x,t)$ is the current, and L and C are the inductance and capacitance per unit length, respectively. By plugging the current propagation function $J(x,t) = J_0 \exp[i(\omega t - kx)]$ into Equation (1), one can obtain the dispersion relation for a transmission line:

$$k^2 = \omega^2 L_\omega C_\omega. \tag{2}$$

For the straight wire, L_ω and C_ω weakly depend on ω. It cannot be treated as an ideal transmission line mode when the ultrashort current signal propagates along a metal wire[51]. As a result, the current dispersion should be considered. If the current propagates in the HC, the longitudinal component of the current can be written as $J_x(x,t) = J_{x0}\exp[i(\omega t - k_x x)]$. Here, k_x is determined by the pitch and radius of the HC, as $k_x = \beta k$, where $\beta = p/2\pi a$ is called the helix radio and p and a are the pitch and radius of the coils, respectively. Therefore, the dispersion relationship for an HC transmission system is as follows:

$$k_x{}^2 = \omega^2 L_a C_a, \tag{3}$$

where L_a and C_a are the equivalent inductance and capacitance of the HC, which are given by Kino and Paik[52] as follows:

$$\begin{aligned} L_a &= \frac{\mu}{2\pi}\frac{k_x{}^2}{\beta^2\gamma^2}\left[I_1(\gamma a)K_1(\gamma a)\right], \\ C_a &= 2\pi/\left[I_0(\gamma a)K_0(\gamma a)\right], \end{aligned} \tag{4}$$

where $\gamma = \left(k_x{}^2 - \omega^2/c^2\right)^{1/2}$, $c = (\mu\varepsilon)^{-1/2}$, and I_n and K_n are the modified Bessel functions of the first and second kind, respectively. Equations (3) and (4) can be simplified as follows:

$$\frac{\omega}{k_x c} = \sqrt{\frac{\beta}{\beta^2 + D}}, \quad D = \frac{I_1(\gamma a)K_1(\gamma a)}{I_0(\gamma a)K_0(\gamma a)}. \tag{5}$$

By solving Equation (5) numerically, we can obtain the surface velocity $v_s = \omega\lambda/2\pi$ of the current at each frequency along an HC or a straight wire (see Figure 2(b)). The surface velocity of the current is related to the frequency of the signal, called current dispersion. In particular, the surface velocity of the lower frequency signal will increase significantly, or signals with frequencies below 100 GHz will have more pronounced dispersion. The main signal frequencies are in this range (Figure 1(c)).

Figure 2(c) shows the spatial-temporal distribution of the current in the HC with pitch $p = 0.5$ mm and radius $a = 0.4$ mm. Unlike in straight Al wire, the current dispersion in the HC is severe. The positive peak of the current becomes wider, and its amplitude decreases with time. Meanwhile, a negative current following the positive current emerges and grows with time (Figure 2(d)). Similar phenomena alternately repeat with the propagation of the current in the HC, making the current waveform dramatically change. Technically, we can define the velocity of the main positive peak as the apparent longitudinal velocity of the current. According to the simulation results, it is linearly fitted to be $v_{CL} = 1.6\beta c$, as shown by the green dashed line in Figure 2(c). It should be noted that this apparent velocity is greater than the expected velocity of $v_0 = \frac{p}{2\pi a}c = \beta c$ for a dispersionless current. In previous studies[27], the parameter of the HC was deliberately chosen so that βc matches the protons' velocities. According to our simulation results, this strategy cannot match the velocities of the traveling field and protons as expected.

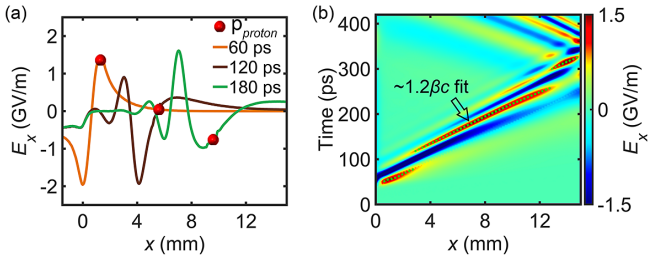

Figure 3. (a) Snapshot of the longitudinal electric field on the central axis of the HC at 60, 120 and 180 ps. The red balls represent the positions of protons with cut-off energy at different times. (b) Spatial-temporal distribution of the longitudinal electric field in an HC, with the mark of the extreme points of positive fields (green dashed lines).

4. Evolution of the electric field and the post-acceleration of protons in a single-stage helical coil

The traveling transient current builds a transient electric field around the wire. In the case of the HC, the field near the center of the coil has a substantial longitudinal component accelerating the protons from the thin foil. In HCPA ignoring current dispersion, Ahmed *et al.*[28] proposed the scheme of stepwise increasing the pitch to handle the synchronization of the electric field and accelerating protons. In their simulation, protons can maintain synchronous acceleration over considerable distances. In our simulation, where current dispersion is considered as it should be, we find that the electric field is constantly changing. Figure 3(a) shows the longitudinal electric field on the central axis of the HC (labeled as E_x) obtained from simulations with $p = 0.5$ mm and $a = 0.4$ mm. At an early time (60 ps), it is a dipole field resulting from a transient current. The amplitude of the first positive field will decrease. Another pulse of the positive field will appear and become stronger (see the brown line). Between the two positive fields is a negative electric field. The field becomes multipole (120 and 180 ps). The red balls indicate the positions of protons with cut-off energy at different times in Figure 3(a). At 120 ps, the electric field experienced by protons with cut-off energy is close to zero. Protons slide from the accelerating phase to the decelerating phase, which we call phase reversal. The protons will accelerate for a short time and then decelerate. The energy gain will be very limited.

In Figure 3(b), the green dashed lines mark the extreme point of the positive E_x in the spatial-temporal distribution. The apparent longitudinal velocity of the positive electric field is fitted to $v_{EL} = 1.2\beta c$. The phase reversals of the positive electric field occur two times in total (shown by the three dashed lines). Whenever a phase reversal occurs, the next positive electric field pulse will be delayed by 2π in phase compared with the previous one. Protons that were accelerated a few ps ago will soon lose acceleration or undergo deceleration. The reversal and delay are abrupt for proton acceleration and cannot be compensated by stepwise increasing the pitch.

We investigate the post-acceleration process of the protons in the evolving electric field in the HC with the constant pitch and radius, $p = 0.5$ mm and $a = 0.4$ mm. Figure 4(a) shows snapshots of the protons' distribution in phase space and the longitudinal electric field at 60, 240 and 360 ps, respectively.

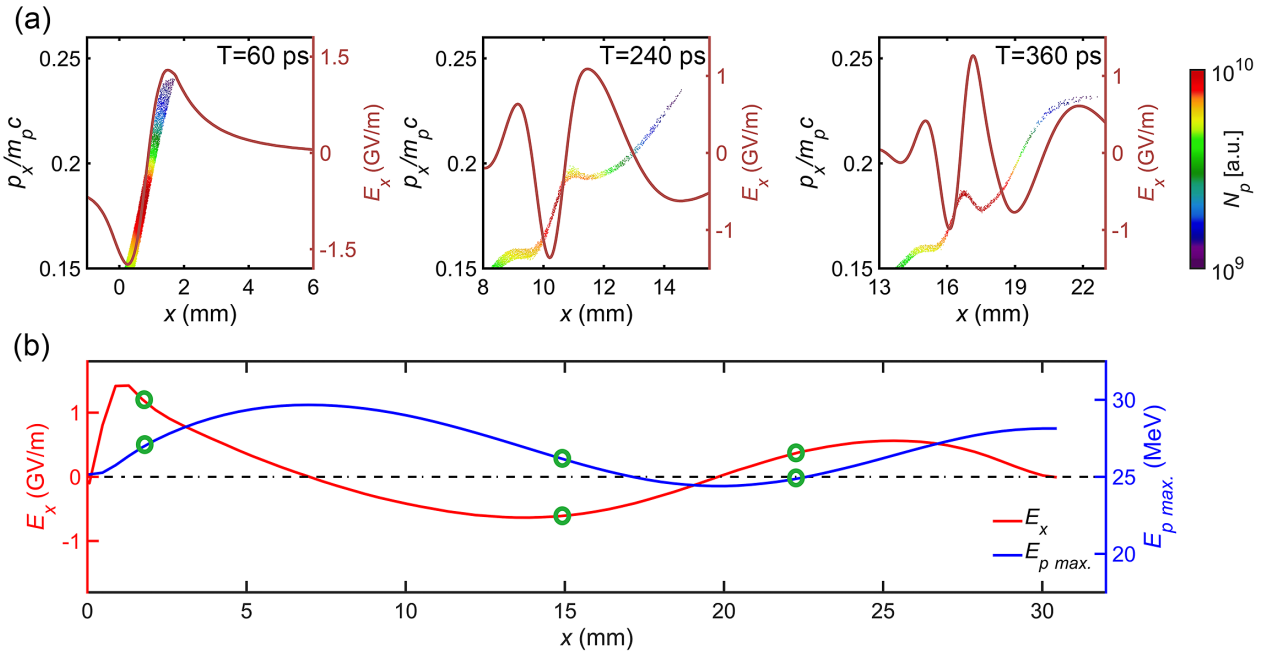

Figure 4. (a) Snapshots of proton distributions in phase space (x, p_x) and the longitudinal electric field at 60, 240 and 360 ps, in a single-stage HC. (b) Longitudinal electric field (red curve) in the coordinate frame of the traveling highest-energy protons, and the evolution of the cut-off energy (blue curve) in a single-stage HC, where the three groups of green circles mark the three statuses in (a).

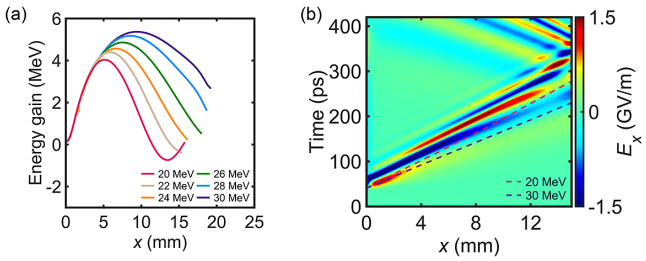

Figure 5. (a) Energy gains of traveling protons in the HC with different input energies. (b) The spatial-temporal distribution of E_x and proton trajectories with input energies of 20 and 30 MeV.

Their initial maximum kinetic energy is 25 MeV. We believe that the protons will be rapidly accelerated to match the apparent speed of the positive electric field of $1.2\beta c$, corresponding to the 28 MeV protons. At $T = 60$ ps, protons at the cut-off energy located at the peak of the positive field undergo the most efficient acceleration. At $T = 240$ ps, the most energetic protons are however in the negative field. In general, most protons experience alternative fields and cannot continuously gain energy. At $T = 360$ ps, the cut-off energy of the protons is even lower than that at $T = 60$ ps. To investigate the energy evolution of the most energetic protons, we show the electric field E_x experienced in their coordinate frame in Figure 4(b). The green circles represent their spatial positions in the three snapshots. Firstly, they are post-accelerated to a maximum energy of 29.7 MeV at $x = 7$ mm in the positive field. They then slide into the negative field and are decelerated to 24.4 MeV. As their velocity decreases, they are 'caught up' by the positive field and accelerated again after $x = 20$ mm. Due to the alternative acceleration and deceleration, the final energy gain is relatively low. The highest energy gain for the most energetic protons, in our case, is 19%, which is comparable to the reported experimental results[21,27,28,34].

We have simulated the energy gains of protons with different input energies from 20 to 30 MeV in the HC, as shown in Figure 5(a). Protons in a wider energy range similarly undergo acceleration and deceleration. Figure 5(b) shows the E_x distribution and the proton trajectories. It is shown that higher-energy protons will be 'caught up' by the negative electric field later, and will obtain higher energy gain, but it is still a faint enhancement. The protons cannot undergo continuous acceleration even if their initial kinetic energy is 30 MeV with injected velocities close to $1.2\beta c$.

In summary, the deceleration stage resulting from the current dispersion drastically undermines the energy gain in the post-acceleration. The second positive electric field is not efficiently utilized. The methods, by continuously or stepwise adjusting the pitch and radius of the HC to extend the accelerated distance[28], cannot eliminate current dispersion and only obtain short-time acceleration. New schemes that consider the current dispersion and can maintain synchronous acceleration for a long time are essential for high-gain post-acceleration.

5. Enhanced post-acceleration in two-stage helical coil post-acceleration

To overcome the problems caused by the current dispersion, we propose a scheme where a two-stage HC is employed, to achieve synchronous acceleration for a long time. The geometry of the two-stage HC is shown in Figure 6(a), where the pitch and radius of the HC are the same as those of the single-stage HC. There is a straight wire between the two

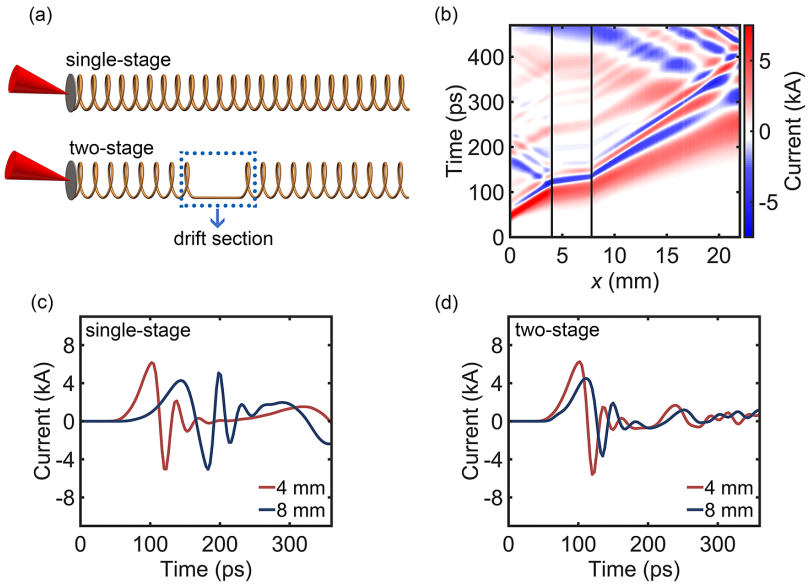

Figure 6. (a) The structure of a single-stage HC and a two-stage HC. (b) The spatial-temporal distribution of the current in the two-stage HC. (c), (d) The temporal profiles of the current pulses at 4 and 8 mm in the case of single- and two-stage HCs, respectively.

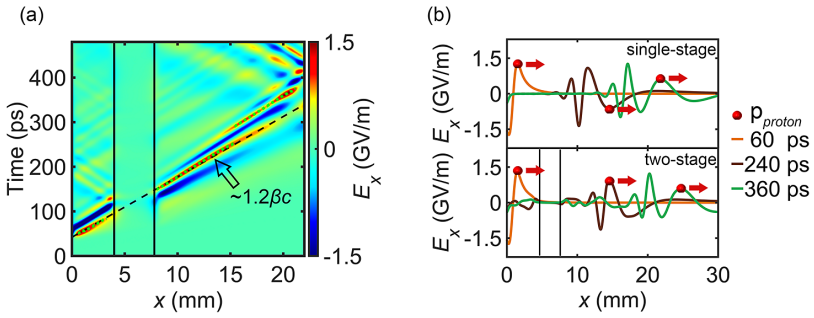

Figure 7. (a) Longitudinal electric field in the two-stage HC, where the black dashed line indicates the velocity mark of $1.2\beta c$ and the green dashed line indicates the extreme points of positive fields. (b) The E_x distribution and the position of protons with initial energy of 25 MeV in single-stage (top) and two-stage (bottom) HCs at 60, 240 and 360 ps, respectively. The red balls represent the protons' positions at the cut-off energy, and the vertical black lines in (a) and (b) indicate the position of the drift section.

coils as the 'drift section'. After the acceleration in the first HC, as shown above, the most energetic protons travel faster than the positive pole of the field and slide into the negative field. In the drift section, the current dispersion becomes milder, and the velocity of the positive current is higher than that of the protons. It is therefore possible to compensate for the phase sliding with appropriate parameters. After the drift section, the protons are in the positive field and begin to be accelerated again in the second HC.

The drift section is introduced at the position of $x = 4$ mm, and the drift section length is chosen as 3.8 mm. The coil parameters are the same as those in a single-stage HC. The reason for this will be discussed later. Figure 6(b) shows the spatial-temporal distribution of the current pulse in the two-stage HC. In the first HC, the current undergoes a strong dispersion. However, in the drift section, its waveform hardly changes as the dispersion is much weaker. It then changes again after entering the second HC. In the drift section, the current travels at a velocity close to c, much faster than the protons. The difference can be seen in Figures 6(c) and 6(d), showing the temporal profiles of current pulses at 4 and 8 mm in the case of single- and two-stage HCs. The current distributions at 4 mm of the single-stage HC and two-stage HC (before the drift section) are the same. However, at 8 mm of the single-stage HC, the current changes significantly, and the negative pulse is greater. At 8 mm in the case of two-stage HC, the current (after the drift section) changes slightly. The gap between the current at 4 and 8 mm is shorter. The current travels faster in the drift section than in the HC.

The spatial-temporal distribution of the electric field E_x is illustrated in Figure 7(a), where the peaks of the positive field are marked by the green dashed lines. The positive electric fields in the first and second stages are seamlessly connected by a straight velocity line of $1.2\beta c$ because the electric field after the drift section is more forward. Figure 7(b) shows the distributions of E_x and the position of the protons with cut-off energy at different times. We need to highlight that the initial positive electric field (60 ps) has been reduced, and the protons can only be subsequently synchronized with the next increased positive electric field. At 240 ps in the case of the single-stage HC, the electric field is relatively backward. The proton is in a negative electric field and is 3.2 mm away from the positive electric field. In the case of the two-stage HC, protons are synchronized with the positive electric field. The drift section in the two-stage HC acts to make the electric field propagate much faster than the protons, and the delayed positive peak is thus able to catch the protons again.

Figure 8(a) shows the protons' distributions in phase space and E_x in the two-stage HC. The high-energy protons are kept in sync with the positive electric field at 60, 240 and 360 ps. As a result, their cut-off energies are significantly improved. Figure 8(b) shows the witnessed E_x of the most energetic protons in their coordinate frames. They are accelerated in the first HC, and the cut-off energy is increased to 29.1 MeV at a position of $x = 4$ mm, slightly lower than that of the single-stage HC. Later, in the drift section, the E_x is weak, and the cut-off energy does not change significantly. In the second HC, they are accelerated over a distance exceeding 20 mm by the second-stage positive field. As a result of the overall acceleration distance of 25 mm, the cut-off energy of the proton beam is increased to 45.1 MeV as compared with the final energy of 28 MeV in Figure 4(b).

It should be noted that the acceleration distance of the protons in the second stage is much longer than in the first stage. In the first stage, the amplitude of the positive electric field is maximum at the beginning (Figure 7(b)). The positive electric field will decrease due to the current dispersion, which is a half-cycle process. In the second-stage HC, the second positive electric field pulse becomes strong and then decreases, which is a full-cycle process. As shown in Figure 6(b), the pulse duration of the current in the second stage is greater than that in the first stage due to the current dispersion. The evolution of the dispersion current will become more stable as the pulse duration expands, as demonstrated by Bardon *et al.*[34]. Therefore, the acceleration of the protons in the second stage can be more stable.

The position and length of the drift section must be carefully designed to compensate for the delay of the electric

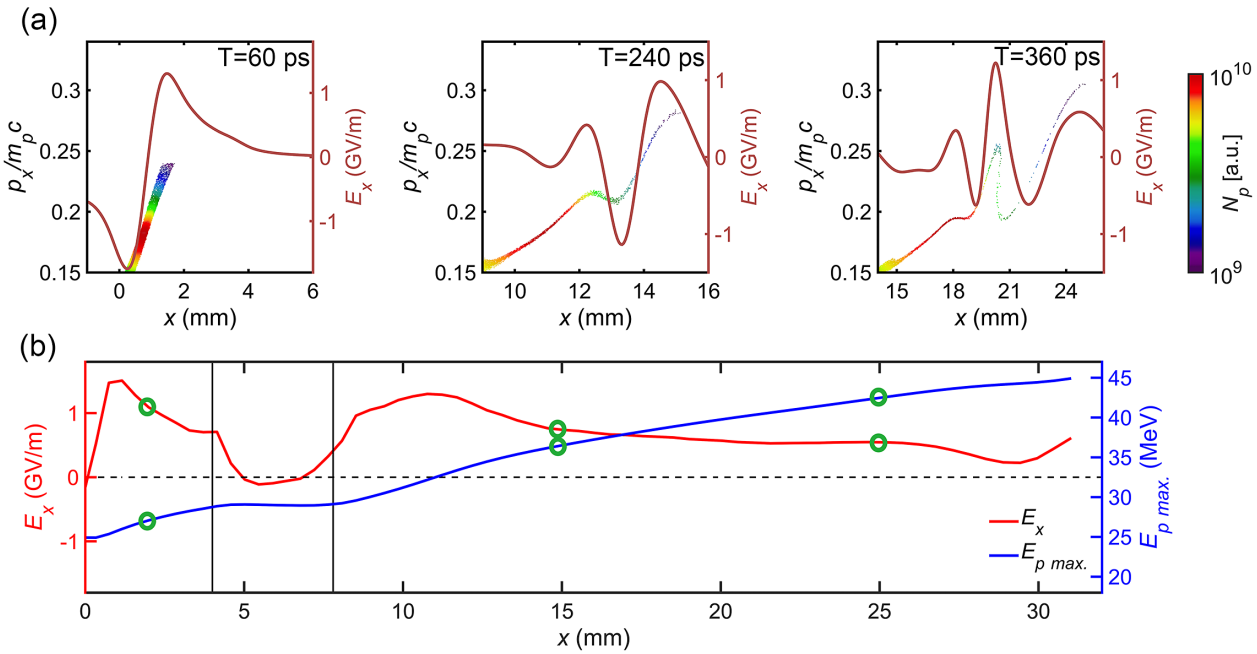

Figure 8. (a) Snapshots of the proton distributions in phase space (x, p_x) and E_x at 60, 240 and 360 ps, in the two-stage HC. (b) Longitudinal electric field (red curve) in the coordinate frames of the traveling protons at the cut-off energy, and the evolution of the cut-off energy (blue curve) in the two-stage HC. The three groups of green circles mark the three snapshots in (a).

field due to the phase reversal. We illustrate snapshots of the E_x of the single-stage HC at different times and mark the spatial positions of protons at cut-off energy in Figure 9(a). The protons represented by the red balls have energies of 28.3, 28.5 and 29.1 MeV at 90, 97 and 102 ps, respectively. At 96 ps, when the most energetic protons are at $x = 4.2$ mm, the first and second positive electric fields are exactly equal. Thereafter, the amplitude of the first positive peak will be exceeded by the second one. This is a good point to introduce a drift section to allow protons to be caught by the second positive field and obtain maximum acceleration. For an integer number of coils turns, we introduce the drift section at $x = 4.0$ mm.

We also vary the length of the single-stage HC and the drift section in the two-stage HC to investigate their energy gains, where the total length of the two-stage HC is kept at 32 mm. As shown in Figure 9(b), the maximum energy gain of the single-stage acceleration is 4.7 MeV with an HC length of 8 mm, which is already longer than the actual acceleration distance of the protons. The maximum energy gain of the two-stage HC reaches 20.1 MeV when the drift length is 3.8 mm. Moreover, energy gain above 15 MeV can be achieved within ±1 mm deviation from the optimum drift length, making it robust for experiments. Figure 9(c) shows the simulated spectrum of the post-accelerated protons after the single-stage and two-stage HC. The primary protons are exponentially distributed with cut-off energy of 25 MeV. It is increased to 29.7 MeV with a single-stage HC of 8 mm length, and the cut-off energy is increased by 19%. Further increasing the length of the single-stage HC to 20 mm does not result in an increase in the energy but rather a reduction. By using the two-stage HC scheme, the acceleration distance can be substantially increased. With the two-stage length of 32 mm, the proton cut-off energy can be increased to 45.1 MeV, an 80.4% increase in cut-off energy, which is four times that of a single-stage HC.

We envision that the two-stage HC scheme can be used for a petawatt-class femtosecond laser to generate high-energy protons for radiotherapy applications. As shown in Figure 10(a), the scaling for escape electron charge as a function of incident laser intensity can be obtained from the model reported by Poye *et al.*[46]. The scaling for the cut-off energy of the protons is derived from the model of Dover *et al.*[47]. The red circles mark the hundreds-of-terawatt laser that we have simulated in the above works. We apply a laser pulse width of 40 fs, a focal spot radius of 6 μm and an absorption coefficient of 40% in the models. It is hoped that a total escape electron charge of 300 nC and a proton cut-off energy of 60 MeV will be generated by a petawatt-class laser with intensity of 3×10^{21} W cm^{-2}(see the red rhombuses in Figure 10(a)). A maximum longitudinal electric field on the HC central axis of 3 GV/m could be formed. Protons with an exponential spectrum of 60 MeV cut-off are injected into the HCs. Based on the simulation results (Figure 10(b)), a cut-off of 72 MeV protons at the output of a single-stage HC would be expected. By employing a two-stage HC scheme, the cut-off energy of protons can be increased to 102 MeV, which is sufficient with a PW-class laser system of Hz-repetition[53] to treat some shallow-seated tumors and most childhood cancers[54].

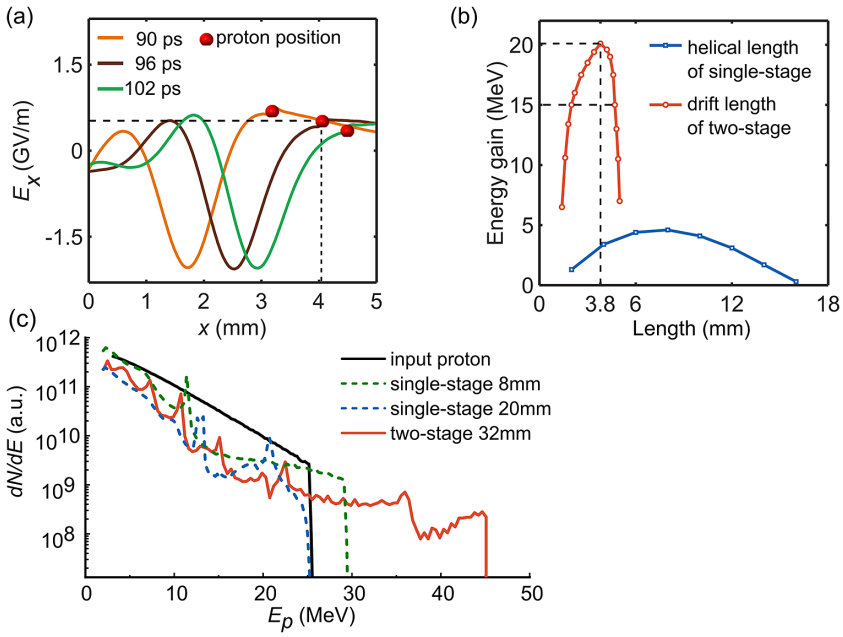

Figure 9. (a) Snapshots of the current distributions and the positions of protons at cut-off energy in the single-stage HC at 90, 96 and 102 ps. (b) Energy gain by varying the helical length of the single-stage HC and the drift length of the two-stage HC. (c) Spectrum of the input protons (black line); spectrum after a single-stage HC of 8 mm (green dashed line) and 20 mm (blue dashed line); spectrum after a two-stage HC (red line).

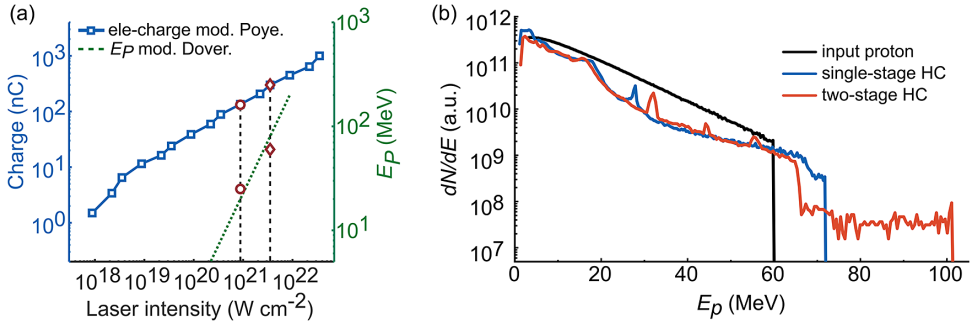

Figure 10. (a) Expected target charge of escaped electrons in the logarithmic scale calculated from the model as a function of laser intensity (blue solid line). The green dashed line shows the cut-off energy of laser-driven protons against laser intensity. The requirements of the hundreds-of-terawatts laser and the petawatt laser in the simulations are marked with red circles and rhombuses, respectively. (b) Spectrum of the input protons in the simulations with the petawatt laser (black line); spectrum after a single-stage HC (blue line); spectrum after a two-stage HC (red line). The lengths of the single-stage HC and two-stage HC are 10 and 40 mm, with $p = 0.55$ mm and $a = 0.3$ mm, respectively, and the drift length is 6.6 mm.

6. Discussion

The above results unambiguously demonstrate that a two-stage HC with a drift section is very beneficial for proton energy enhancement. An interesting question would be the following: given that current dispersion and phase change could be controlled by the drift section, can a multi-stage scheme (over two stages) be applied to achieve longer distance synchronization and thus continue to boost proton energy?

We find that the energy enhancement in a multi-stage HC will be constrained by the impedance mismatch between the coils and the drift sections. The impedance mismatch will cause a current reflection at the connection point between the coil and the drift section, as shown in Figure 11(a). The reflected current will superimpose on the original pulse to form a pulse train, called reflection ringing (RR)[55]. We first conduct simulations of the current and the electric field in a structure consisting of three HC segments based on the hundreds-of-terawatts laser. The current will be reflected when it enters the drift section from the coil, resulting in disruption and weakening of the current (see Figure 11(b)). In the third HC, the current distribution will become much more complex due to the development of dispersion and RR.

The longitudinal electric field is also affected. We build the three-stage HC on the basis of the two-stage HC according to the strategy previously described. The second drift section is introduced when the third positive electric field equals the second one. The delay between each positive electric field could be compensated as they coincide with the black

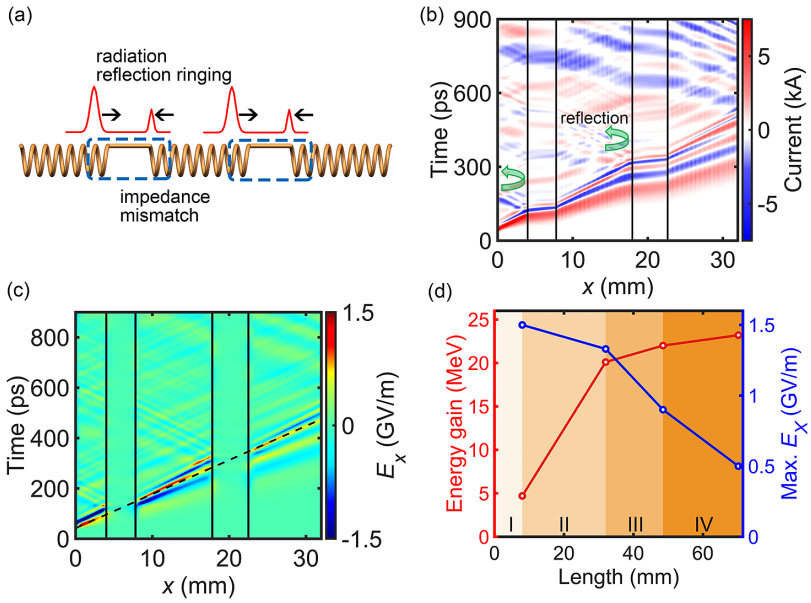

Figure 11. (a) Scheme of the reflection ringing of a three-stage HC structure. (b) Spatial-temporal distribution of the current in a three-stage HC. (c) Spatial-temporal distribution of E_x in a three-stage HC, where the black dashed lines in (c) mark the velocity of $1.2\beta c$ and the vertical black lines in (b) and (c) represent drift sections. (d) Energy gain (red curve) and maximum intensity of E_x (blue curve) at different stages of the HC (from one to four stages in different yellow regions).

dashed line in Figure 11(c). The synchronous acceleration of protons is maintained. However, the waveform of the electric field becomes more turbulent, and its strength decreases simultaneously. We check the energy gain from single-stage to four-stage HCs separately in Figure 11(d). The blue curve shows the maximum strength of E_x in different stages. It is observed that the electric field decreases rapidly as the number of stages increases, with only 0.5 GV/m in the fourth HC. As a result, the energy gain can be significantly increased to 20.1 MeV in the second HC, but modestly increased to 22 or 23.2 MeV in the third or fourth HC, even though the total HC length has been doubled.

7. Conclusion

We demonstrate a dispersion-controlled scheme to enhance the energy of post-acceleration protons using a two-stage HC structure. The cut-off energy is improved from 25 to 45.1 MeV with a hundreds-of-terawatts laser, four times higher than that of the single-stage HC. Over 100 MeV protons can be obtained using a petawatt laser. Based on the self-consistent simulations and the circuit transmission model, we reveal for the first time in detail how the transient current pulses disperse in an HC, causing phase sliding and reversal in the electric field, and how the protons become desynchronous with the acceleration field. With a two-stage HC structure, the current travels faster in the drift section and can compensate for the dispersion-induced delay, thus enabling the proton and accelerated field to synchronize again. In conclusion, the two-stage scheme is a simple and practical way to control the current dispersion of HCPA to enhance the energy gain of laser-driven ions, which is promising for the application of oncological therapy[56].

Acknowledgement

This work was supported by the NSFC Innovation Group Project (No. 11921006), the National Grand Instrument Project (No. 2019YFF01014402), and the Guangdong Provincial Science and Technology Plan Project (No. 2021B0909050006). W. Ma acknowledges support from the National Science Fund for Distinguished Young Scholars (No. 12225501).

References

1. H. Daido, M. Nishiuchi, and A. S. Pirozhkov, Rep. Prog. Phys. **75**, 056401 (2012).
2. A. Macchi, M. Borghesi, and M. Passoni, Rev. Mod. Phys. **85**, 751 (2013).
3. J. Badziak, Opto-Electron. Rev. **15**, 1 (2007).
4. M. Borghesi, J. Fuchs, S. V. Bulanov, A. J. Mackinnon, P. K. Patel, and M. Roth, Fusion Sci. Technol. **49**, 412 (2006).
5. F. Nurnberg, M. Schollmeier, E. Brambrink, A. Blazevic, D. C. Carroll, K. Flippo, D. C. Gautier, M. Geissel, K. Harres, B. M. Hegelich, O. Lundh, K. Markey, P. McKenna, D. Neely, J. Schreiber, and M. Roth, Rev. Sci. Instrum. **80**, 033301 (2009).
6. J. R. Rygg, F. H. Seguin, C. K. Li, J. A. Frenje, M. J. Manuel, R. D. Petrasso, R. Betti, J. A. Delettrez, O. V. Gotchev, J. P. Knauer, D. D. Meyerhofer, F. J. Marshall, C. Stoeckl, and W. Theobald, Science **319**, 1223 (2008).
7. F. Kroll, F. E. Brack, C. Bernert, S. Bock, E. Bodenstein, K. Brüchner, T. E. Cowan, L. Gaus, R. Gebhardt, U. Helbig, L. Karsch, T. Kluge, S. Kraft, M. Krause, E. Lessmann, U.

Masood, S. Meister, J. Metzkes-Ng, A. Nossula, J. Pawelke, J. Pietzsch, T. Püschel, M. Reimold, M. Rehwald, C. Richter, H. P. Schlenvoigt, U. Schramm, M. E. P. Umlandt, T. Ziegler, K. Zeil, and E. Beyreuther, Nat. Phys. **18**, 316 (2022).
8. J. Han, Z. Mei, C. Lu, J. Qian, Y. Liang, X. Sun, Z. Pan, D. Kong, S. Xu, and Z. Liu, Front. Cell Dev. Biol. **9**, 672929 (2021).
9. M. Barberio, M. Scisciò, S. Vallières, F. Cardelli, S. Chen, G. Famulari, T. Gangolf, G. Revet, A. Schiavi, and M. Senzacqua, Nat. Commun. **9**, 372 (2018).
10. D. Kong, S. Xu, Y. Shou, Y. Gao, Z. Mei, Z. Pan, Z. Liu, Z. Cao, Y. Liang, Z. Peng, P. Wang, D. Luo, Y. Li, Z. Li, H. Xie, G. Zhang, W. Luo, J. Zhao, S. Chen, Y. Geng, Y. Zhao, J. Xue, X. Yan, and W. Ma, Laser Part. Beams **2022**, 1 (2022).
11. P. Mora, Phys. Rev. Lett. **90**, 185002 (2003).
12. D. Margarone, O. Klimo, I. J. Kim, J. Prokupek, J. Limpouch, T. M. Jeong, T. Mocek, J. Psikal, H. T. Kim, J. Proska, K. H. Nam, L. Stolcova, I. W. Choi, S. K. Lee, J. H. Sung, T. J. Yu, and G. Korn, Phys. Rev. Lett. **109**, 234801 (2012).
13. F. Wagner, O. Deppert, C. Brabetz, P. Fiala, A. Kleinschmidt, P. Poth, V. A. Schanz, A. Tebartz, B. Zielbauer, M. Roth, T. Stohlker, and V. Bagnoud, Phys. Rev. Lett. **116**, 205002 (2016).
14. N. P. Dover, M. Nishiuchi, H. Sakaki, K. Kondo, H. F. Lowe, M. A. Alkhimova, E. J. Ditter, O. C. Ettlinger, A. Y. Faenov, M. Hata, G. S. Hicks, N. Iwata, H. Kiriyama, J. K. Koga, T. Miyahara, Z. Najmudin, T. A. Pikuz, A. S. Pirozhkov, A. Sagisaka, U. Schramm, Y. Sentoku, Y. Watanabe, T. Ziegler, K. Zeil, M. Kando, and K. Kondo, High Energy Density Phys. **37**, 100847 (2020).
15. J. Schreiber, F. Bell, F. Gruner, U. Schramm, M. Geissler, M. Schnurer, S. Ter-Avetisyan, B. M. Hegelich, J. Cobble, E. Brambrink, J. Fuchs, P. Audebert, and D. Habs, Phys. Rev. Lett. **97**, 045005 (2006).
16. E. L. Clark, K. Krushelnick, M. Zepf, F. N. Beg, M. Tatarakis, A. Machacek, M. I. Santala, I. I. Watts, P. A. Norreys, and A. E. Dangor, Phys. Rev. Lett. **85**, 1654 (2000).
17. M. Alien, Y. Sentoku, P. Audebert, A. Blazevic, T. Cowan, J. Fuchs, J. C. Gauthier, M. Geissel, M. Hegelich, S. Karsch, E. Morse, P. K. Patel, and M. Roth, Phys. Plasmas **10**, 3283 (2003).
18. L. Robson, P. T. Simpson, R. J. Clarke, K. W. D. Ledingham, F. Lindau, O. Lundh, T. McCanny, P. Mora, D. Neely, C. G. Wahlstrom, M. Zepf, and P. McKenna, Nat. Phys. **3**, 58 (2007).
19. J. Fuchs, P. Antici, E. D'Humieres, E. Lefebvre, M. Borghesi, E. Brambrink, C. A. Cecchetti, M. Kaluza, V. Malka, M. Manclossi, S. Meyroneinc, P. Mora, J. Schreiber, T. Toncian, H. Pepin, and R. Audebert, Nat. Phys. **2**, 48 (2006).
20. H. Schwoerer, S. Pfotenhauer, O. Jackel, K. U. Amthor, B. Liesfeld, W. Ziegler, R. Sauerbrey, K. W. Ledingham, and T. Esirkepov, Nature **439**, 445 (2006).
21. S. Kar, H. Ahmed, R. Prasad, M. Cerchez, S. Brauckmann, B. Aurand, G. Cantono, P. Hadjisolomou, C. L. S. Lewis, A. Macchi, G. Nersisyan, A. P. L. Robinson, A. M. Schroer, M. Swantusch, M. Zepf, O. Willi, and M. Borghesi, Nat. Commun. **7**, 10792 (2016).
22. J.-L. Dubois, F. Lubrano-Lavaderci, D. Raffestin, J. Ribolzi, J. Gazave, A. C. La Fontaine, E. d'Humières, S. Hulin, P. Nicolaï, and A. Poyé, Phys. Rev. E **89**, 013102 (2014).
23. S. Tokita, S. Sakabe, T. Nagashima, M. Hashida, and S. Inoue, Sci. Rep. **5**, 8268 (2015).
24. P. McKenna, D. C. Carroll, R. J. Clarke, R. G. Evans, K. W. Ledingham, F. Lindau, O. Lundh, T. McCanny, D. Neely, A. P. Robinson, L. Robson, P. T. Simpson, C. G. Wahlstrom, and M. Zepf, Phys. Rev. Lett. **98**, 145001 (2007).
25. F. Consoli, V. T. Tikhonchuk, M. Bardon, P. Bradford, D. C. Carroll, J. Cikhardt, M. Cipriani, R. J. Clarke, T. E. Cowan, and C. N. Danson, High Power Laser Sci. Eng. **8**, e22 (2020).
26. H. B. Zhuo, S. J. Zhang, X. H. Li, H. Y. Zhou, X. Z. Li, D. B. Zou, M. Y. Yu, H. C. Wu, Z. M. Sheng, and C. T. Zhou, Phys. Rev. E **95**, 013201 (2017).
27. H. Ahmed, S. Kar, G. Cantono, P. Hadjisolomou, A. Poye, D. Gwynne, C. Lewis, A. Macchi, K. Naughton, and G. Nersisyan, Sci. Rep. **7**, 10891 (2017).
28. H. Ahmed, P. Hadjisolomou, K. Naughton, A. Alejo, S. Brauckmann, G. Cantono, S. Ferguson, M. Cerchez, D. Doria, J. Green, D. Gwynne, T. Hodge, D. Kumar, A. Macchi, R. Prasad, O. Willi, M. Borghesi, and S. Kar, Sci. Rep. **11**, 699 (2021).
29. S. Ferguson, P. Martin, H. Ahmed, E. Aktan, M. Alanazi, M. Cerchez, D. Doria, J. S. Green, B. Greenwood, B. Odlozilik, O. Willi, M. Borghesi, and S. Kar, New J. Phys. **25**, 013006 (2023).
30. A. Poye, J. L. Dubois, F. Lubrano-Lavaderci, E. D'Humieres, M. Bardon, S. Hulin, M. Bailly-Grandvaux, J. Ribolzi, D. Raffestin, J. J. Santos, P. Nicolai, and V. Tikhonchuk, Phys. Rev. E **92**, 043107 (2015).
31. H. Ahmed, S. Kar, A. Giesecke, D. Doria, G. Nersisyan, O. Willi, C. Lewis, and M. Borghesi, High Power Laser Sci. Eng. **5**, e4 (2017).
32. E. Aktan, H. Ahmed, B. Aurand, M. Cerchez, A. Poye, P. Hadjisolomou, M. Borghesi, S. Kar, O. Willi, and P. Prasad, Phys. Plasmas **26**, 070701 (2019).
33. K. Quinn, P. A. Wilson, C. A. Cecchetti, B. Ramakrishna, L. Romagnani, G. Sarri, L. Lancia, J. Fuchs, A. Pipahl, T. Toncian, O. Willi, R. J. Clarke, D. Neely, M. Notley, P. Gallegos, D. C. Carroll, M. N. Quinn, X. H. Yuan, P. McKenna, T. V. Liseykina, A. Macchi, and M. Borghesi, Phys. Rev. Lett. **102**, 194801 (2009).
34. M. Bardon, J. G. Moreau, L. Romagnani, C. Rousseaux, M. Ferri, F. Lefevre, I. Lantuejoul, B. Etchessahar, S. Bazzoli, D. Farcage, H. Maskrot, F. Serres, M. Chevrot, E. Loyez, E. Veuillot, W. Cayzac, B. Vauzour, G. Boutoux, G. Sary, A. C. La Fontaine, L. Gremillet, A. Poye, E. D. Humieres, and V. T. Tikhonchuk, Plasma Phys. Controll. Fusion **62**, 125019 (2020).
35. K. Jiang, C. T. Zhou, T. W. Huang, L. B. Ju, C. N. Wu, L. Li, H. Zhang, S. Z. Wu, T. X. Cai, B. Qiao, M. Y. Yu, and S. C. Ruan, Plasma Phys. Controll. Fusion **61**, 075004 (2019).
36. S. Kar, H. Ahmed, G. Nersisyan, S. Brauckmann, F. Hanton, A. L. Giesecke, K. Naughton, O. Willi, C. L. S. Lewis, and M. Borghesi, Phys. Plasmas **23**, 055711 (2016).
37. D. M. Sullivan, *Electromagnetic Simulation Using the FDTD Method* (John Wiley & Sons, Hoboken, NJ, 2013).
38. O. Cessenat, arXiv:1301.4539 (2013).
39. H. Spachmann and U. Becker, Nucl. Instrum. Methods Phys. Res. Sect. A **558**, 50 (2006).
40. W. Kuropka, F. Mayet, R. Aßmann, and U. Dorda, Nucl. Instrum. Methods Phys. Res. Sect. A **909**, 193 (2018).
41. https://www.3ds.com/products-services/simulia/products/cst-studio-suite/.
42. A. J. Mackinnon, Y. Sentoku, P. K. Patel, D. W. Price, S. Hatchett, M. H. Key, C. Andersen, R. Snavely, and R. R. Freeman, Phys. Rev. Lett. **88**, 215006 (2002).
43. M. Tampo, S. Awano, P. R. Bolton, K. Kondo, K. Mima, Y. Mori, H. Nakamura, M. Nakatsutsumi, R. B. Stephens, K. A. Tanaka, T. Tanimoto, T. Yabuuchi, and R. Kodama, Phys. Plasmas **17**, 073110 (2010).
44. M. Afshari, J. Hornung, A. Kleinschmidt, P. Neumayer, D. Bertini, and V. Bagnoud, AIP Adv. **10**, 035023 (2020).
45. D. A. Maclellan, D. C. Carroll, R. J. Gray, N. Booth, B. Gonzalez-Izquierdo, H. W. Powell, G. G. Scott, D. Neely, and P. McKenna, Laser Part. Beams **31**, 475 (2013).
46. A. Poye, S. Hulin, M. Bailly-Grandvaux, J. L. Dubois, J. Ribolzi, D. Raffestin, M. Bardon, F. Lubrano-Lavaderci, E. D'Humieres, J. J. Santos, P. Nicolai, and V. Tikhonchuk, Phys. Rev. E **91**, 043106 (2015).

47. N. P. Dover, M. Nishiuchi, H. Sakaki, K. Kondo, M. A. Alkhimova, A. Y. Faenov, M. Hata, N. Iwata, H. Kiriyama, J. K. Koga, T. Miyahara, T. A. Pikuz, A. S. Pirozhkov, A. Sagisaka, Y. Sentoku, Y. Watanabe, M. Kando, and K. Kondo, Phys. Rev. Lett. **124**, 084802 (2020).
48. A. Poyé, S. Hulin, J. Ribolzi, M. Bailly-Grandvaux, F. Lubrano-Lavaderci, M. Bardon, D. Raffestin, J. Santos, and V. Tikhonchuk, Phys. Rev. E **98**, 033201 (2018).
49. T. Itoh and C. Caloz, *Electromagnetic Metamaterials: Transmission Line Theory and Microwave Applications* (John Wiley & Sons, Hoboken, NJ, 2005).
50. S. Ramo, J. R. Whinnery, and T. Van Duzer, *Fields and Waves in Communication Electronics* (John Wiley & Sons, Hoboken, NJ, 1994).
51. E. Afshari, H. S. Bhat, A. Hajimiri, and J. E. Marsden, J. Appl. Phys. **99**, 054901 (2006).
52. G. S. Kino and S. F. Paik, J. Appl. Phys. **33**, 3002 (1962).
53. C. N. Danson, C. Haefner, J. Bromage, T. Butcher, J. C. F. Chanteloup, E. A. Chowdhury, A. Galvanauskas, L. A. Gizzi, J. Hein, D. I. Hillier, N. W. Hopps, Y. Kato, E. A. Khazanov, R. Kodama, G. Korn, R. X. Li, Y. T. Li, J. Limpert, J. G. Ma, C. H. Nam, D. Neely, D. Papadopoulos, R. R. Penman, L. J. Qian, J. J. Rocca, A. A. Shaykin, C. W. Siders, C. Spindloe, S. Szatmari, R. M. G. M. Trines, J. Q. Zhu, P. Zhu, and J. D. Zuegel, High Power Laser Sci. Eng. **7**, e54 (2019).
54. K. D. Wang, K. Zhu, M. J. Easton, Y. J. Li, C. Lin, and X. Q. Yan, Phys. Rev. Accel. Beams **23**, 111302 (2020).
55. Y. Chung, M. Cho, and H. Lim, IEEE Trans. Vehicular Technol. **71**, 9375 (2022).
56. J. Fuchs, P. Audebert, M. Borghesi, H. Pépin, and O. Willi, C. R. Phys. **10**, 176 (2009).